# Template free mild hydrothermal fabrication of size-controlled core-shell CuO@Cu2O visible light photocatalyst, structural stability and their interfacial charge transfer mechanistic investigation

# Template free mild hydrothermal fabrication of size-controlled core-shell CuO@Cu₂O visible light photocatalyst, structural stability and their interfacial charge transfer mechanistic investigation

Sekar Karthikeyan, [†] Chitiphon Chuaicham, [†] Radheshyam R Pawar, [†] Keiko Sasaki, [†]* Wei Li, [‡] Adam F. Lee,[‖] Karen Wilson,[‖]

[†]Department of Earth Resources Engineering, Faculty of Engineering, Kyushu University, 744 Motooka, Nishiku, Fukuoka 819-0395, Japan

[‡]European Bioenergy Research Institute, Aston University, Birmingham B4 7ET, UK

[‖]Applied Chemistry & Environmental Science, RMIT University, Melbourne VIC 3000, Australia.

*Corresponding Author
Prof. Keiko Sasaki, E-mail: keikos@mine.kyushu-u.ac.jp, Tel & Fax: +81-92-802-3338

## Abstract

Solar-driven photocatalytic processes rely on potential method for clean environment and environmental remediation. Semiconducting copper oxides ($Cu_2O$, $CuO$) photocatalysts showed efficient solar energy conversion applications in the visible light by tuning the structural and electronic properties. To understand the structure-function-relationship and stability of the photocatalysts, we have demonstrated low hydrothermal template free synthesis of hollow, hierarchical, core-shell $CuO@Cu_2O$, $Cu_2O$, $Cu/CuO@Cu_2O$ architecture by low hydrothermal with size ranges from 200 nm to 2μm. The superior activity and stability of the photocatalysts investigated by N-acetyl-para-aminophenol (as a model pharmaceutical organic compound) under visible light. The photocatalyst surface/bulk electronic properties and mechanistic investigation as well as the stability was investigated by surface oxidation states, apparent quantum efficiency, and rates of charge recombination as well as the efficiency competing with other bench mark reports. This work anticipated to provide significant insight of constructing other core-shell/hollow, hierarchical structures for variety of solar-driven photocatalytic energy conversion applications with high-performance.

***Keywords:*** *Core-shell CuO/Cu₂O; hierarchical, photocatalysis; N-acetyl-para-aminophenol, visible light.*

## 1. Introduction

Recently, solar energy utilization from semiconductors has great attention and potential technology for solar energy, clean environment and fine chemical production applications. Last few decades, $TiO_2$ is considered most promising bench mark photocatalyst for efficient solar energy utilization in various applications such as solar fuels, environmental remediation, microorganism inactivation, and personal care products[1]. However, titanium dioxide activates only 5% of the UV light region, which limits the successful practical application[2]. Copper oxide ($Cu_2O$) is an economical and earth abundant p-type semiconductor (band gap 2.0 to 2.2 eV) with favourable conduction and valence bands position for effective photocatalytic activity towards visible region[3]. The unique electronic properties of $Cu_2O$ have

high absorption coefficient, excellent conductivity, and high photocatalytic activity for solar fuel conversion, water splitting and environmental remediation. Research strategy engineering the $Cu_2O$ physicochemical, electronic and surface/interface properties by controlling sizes[4], structures[5], co-catalyst loading[6], hetero junctions[7], and crystal facet frameworks[8] for favourable light absorption on the extended axial route, prolong life time and an efficient charge separation between the interface and the axial direction towards efficient photoconversion applications. but poor quantum efficiency and the stability[9]. Cupric oxide (CuO, band gap 1.2 to 1.7 eV) is an excellent co-catalyst can improve the kinetic stability of $Cu_2O$ as well as efficiently improve the charge separation to minimize the electron hole-pair recombination between the interface of $CuO/Cu_2O$, which accelerated the favourable valence band potential and enhance the charge transport facility and minimizing electron-hole pair recombination of photoinduced electrons between the interface[10, 11]. Design nanostructures, core-shell/hollow, hierarchical architectures have multifunctional characteristics, synergistic surface, quantum confinement, quantum coherence, interface effects and excellent stability for higher catalytic, photocatalytic and electrochemical performances [12-14]. To date, reports on core-shell/hollow $Cu/Cu_2O$, $CuO/Cu_2O$ hybrids synthesised by various approaches such as template assisted electrodeposition[15], high temperatures (<450 °C) [16, 17], toluene assisted high temperature 200 °C for 12−48 h[12], template free hydrothermal 200 °C[18], size controlled but high temperature 270°C[19], template assisted size controlled (230 to 260 nm) $Cu_2O$ hollow[20], bilayer $Cu_2O/CuO$ by double-potential pulse chronoamperometric deposition[21], DMF with high temperature 150 to 210 °C[22]. **Chen et al. 2018** reported two spatially separated location of the surface (built-in electric field) having potential candidate for efficiency electron-hole (e⁻-h⁺) pair separation, fast charge carrier transport and advantages for wider chemical reactions [23]. **Yang et al. 2016** reported the heterojunction between $Cu_2O/CuO$ the photogenerated e⁻ in conduction band (CB) of copper (I) oxide transferred to CB of CuO at $Cu_2O/CuO$ interface; meanwhile, the leaving positive holes in CuO are transferred to $Cu_2O$ under visible-light irradiation[21]. However, core-shell/hollow $CuO/Cu_2O$ architectures and their solar-driven photoreactions were very rarely described in the above previous reports. Based on our previous report[4], well defined $Cu_2O$ nanocube with size ranges (50 to 500 nm) and the highest phenol photocatalytic activity was achieved 300 to 500 nm.

Here we demonstrated the continued interest for systematic study of their corresponding size-structure-activity relationships by new synthetic route fabrication of hollow, hierarchical, core-shell $CuO@Cu_2O$, $Cu_2O$, $Cu/CuO@Cu_2O$ architecture by low hydrothermal with size ranges from 200 nm to 2μ and their corresponding photocatalytic properties. The physicochemical, surface and bulk electronic properties, optical band gaps, electronic band energies were characterised by diverse analytical techniques such as XANES, XRD, STEM-elemental mapping, HRTEM, XPS, $N_2$ porosimetry, SEM, DRUVS, photoluminescence spectroscopy etc., The complete mechanistic investigation as well as stability of the photocatalysts investigated by APAP under visible light by surface oxidation state of copper, apparent

quantum efficiency, and rates of charge recombination as well as the efficiency compared with other reports. This report gives significant insight of core-shell/hollow structured high-performance materials by simple one pot synthesis potential for clean environment application, not limited other photocatalytic applications.

## 2. Experimental

### 2.1. Chemicals

Copper (II) chloride dihydrate ($CuCl_2.2H_2O$ Sigma, 97%), polyethylene glycol (Wako, Average molecular weight: 560 to 640), sodium hydroxide (NaOH, 98% Wako), hydrazine monohydrate ($H_4N_2.H_2O$, 98% Wako), ethanol (99.5%, Wako), Acetonitrile, 99.8% (Wako, Japan), HPLC water (Wako, Japan), (N-acetyl-para-aminophenol or Paracetamol (4-hydroxyacetnilide, $C_8H_9NO_2$, 98%; TCI, Japan).

### 2.2. Fabrication of Core-Shell CuO@Cu$_2$O photocatalyst

A Core-Shell CuO@Cu$_2$O photocatalyst was fabricated by a simple template free low hydrothermal method. Typically, 50 mL of 0. 2 M copper chloride dihydrate and 3 mL of 0.01 M PEG-600 along with 6mL of water by magnetic stirring speed at 600 rpm and 60 °C for 10 min, resulting reaction mixtures were observed in deep blue solution. Simultaneously, mixture of 10 mL of 2 M NaOH and 1mL of 2M hydrazine monohydrate ($H_4N_2.H_2O$) with 10 mL D.I. water added dropwise to the above reaction and stirring continued another 15 min. Then post reaction mixtures were transferred to a sealed round bottom flask under $N_2$ for 30 min to allow formation of a yellowish-red CuO@Cu$_2$O precipitate. Then precipitate of CuO@Cu$_2$O catalyst washed three times with water followed by ethanol three times to make sure removal any residual PEG and centrifugation for 6 min at 10000 rpm, and then freeze dried for 24h; named as Cu$_2$O-B and stored in desiccator. The core-shell formation mechanism, the PEG and $CuCl_2.2H_2O$ initiate reaction to complexation of Cu (II) ions are then precipitated in the form of Cu (I) oxide and Cu (II) oxide in the presence of NaOH and hydrazine monohydrate addition.
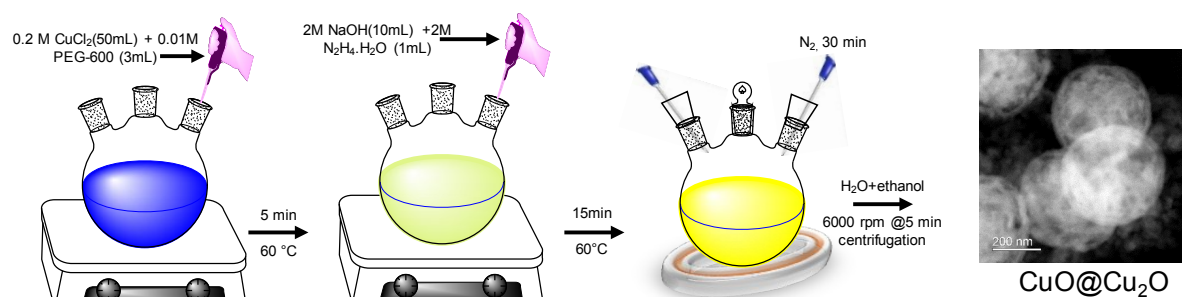


***Scheme 1:*** *Synthesis scheme of Core-Shell CuO@Cu$_2$O*

The schematic illustration of CuO@Cu$_2$O synthetic scheme processes showed in **Scheme. 1.**

$$4CuCl_2 + N_2H_4.H_2O + 8NaOH \rightarrow 2Cu_2O + N_2 + 8NaCl + 7H_2O \tag{1}$$
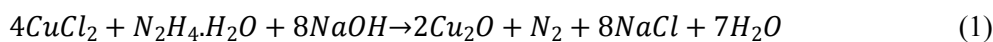
The hydroxyl groups in PEG compound at 60°C are possible to control the Cu ions dimensions, which results core-shell CuO@Cu$_2$O catalyst. In above schematic reaction, the Cu (II) ions are converted into to Cu (I) and Cu(II) ions and subsequently oxidized to form CuO/Cu$_2$O spherical particles in presence of reducing and stabilizing agents. The formation spherical particles have to self-aggregate presence of N$_2$ around the liquid-gas interface to form core-shell structures, and other structures and size varied by controlling PEG concentration and reducing agent. For Cu$_2$O-A (same above method was followed as Cu$_2$O-B, only hydrazine monohydrate was 0.5mL). For Cu$_2$O-C reducing agent concentration was 1M (0.5mL) and addition of reagents, first sodium hydroxide followed by reducing agent. For Cu$_2$O-D, same procedure as Cu$_2$O-C, and amount of PEG was 0.5mL.

### 2.3. N-acetyl-para-aminophenol (APAP) photodegradation experiment

20 mg of photocatalysts dispersed 50 mL of APAP aqueous solution (0.06 mM) and then sonicated 5 min for complete dispersion was transferred to 250 mL photoreactor. Prior light illumination above this mixture was continued stirring in dark to make sure any adsorption. After adsorption, aliquots were collected for HPLC analysis, and then started light illumination reaction with 500 W Xe lamp with a cut-off filter 420 nm under visible light (temperature maintained 25° C, stirring speed RPM was maintained 500; light intensity 1.82 mV/cm², effective irradiation area 4.5 cm and distance from light source to reaction mixture is 14. 9 cm). Aliquots were collected at different time intervals and filtered using CPO20AN filter for all samples including initial samples by standard calibration by HPLC.

For APAP concentration:

$$APAP\ (\%) = \frac{APAP\ intial - APAP\ final}{APAP\ initial} \times 100 \tag{2}$$

Where, 'initial and final' is the molar concentration of N-acetyl-para-aminophenol.

$$Quantum\ efficiency\ (\%) = \frac{APAP\ removal\ rate}{Neins} \times 100 \tag{3}$$

Quantum efficiency calculations (**supporting information eqs: S1-S6**)

### 2.4. HPLC calibration

APAP was analysed using a high performance liquid chromatography system (JASCO UV plus 2075 serious, Japan)) coupled with an intelligent UV/Vis detector selected at λ=243 nm and a Shodex C18M4E analytical column (4.6 I.D × 250mm), separation factor (α1=2.42 and α2=1.47) with a constant temperature of 25°C and pressure maximum 20 MPa, pressure minimum 0.2 MPa. The eluent consists of 30:70 (v/ v) acetonitrile: water (Wako, Japan) with a flow rate of 0.6mL/min.

### 2.5. X-ray absorption near edge structure (XANES)

XANES spectra of the synthesised core-shell catalysts and standard substances (Cu-metal, $Cu_2O$ and CuO) were measured using an ionization chamber in transmission mode for Cu K-edge using a silicon drift detector (SDD) on a BL15 at the Kyushu Synchrotron Light Research Center (SAGA-LS; Tosu, Japan). The samples were prepared by mixing with boron nitride for this measurement.

The photon energy was scanned using Si double crystal monochromator with high energy resolution Cu K-edge in the range from 8.9 to 9.2 keV for the Cu K-edge. The operation current of 171.9 mA and the electronic energy of 1.40 GeV received in electronic accelerator from storage ring. The linear combination fitting (LCF) analysis of all sample were done by Athena-Demeter 0.9.26 program in the Demeter computer package.

### 2.6. Core-Shell CuO@Cu₂O Characterization

### (supporting information)

### 3. Results and discussion

The electronic and optical absorption properties of core-shell CuO@$Cu_2O$ was calculated from solid state DRS-UV spectroscopy. **Fig.1a** showed the solid state DRS-UV of core-shell CuO@$Cu_2O$ photocatalysts broad absorbance around 200-600 nm assigned to copper oxides region, which is close agreement with our previous report [4], and corresponding band gaps calculated from Tauc plots presented in **Fig.S1** and the calculation was made using Eq. (4):
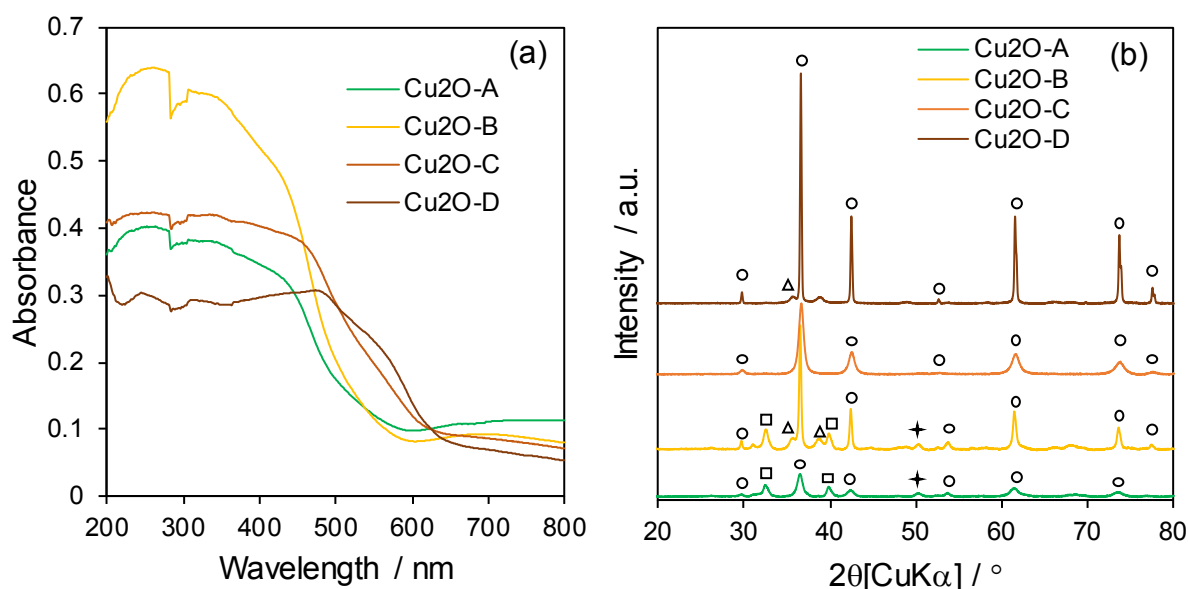


**Fig. 1** a) solid state DRS-UV, b**)** XRD pattern core-shell CuO@$Cu_2O$ photocatalyst

( ○ $Cu_2O$, ▲ CuO, □ $Cu_2(OH)Cl$, ✦ Cu)

$$\alpha h v = A(h v - E_g)^\eta \tag{4}$$

5

Where, $A$ is absorption coefficient, $\alpha$ is linear absorption coefficient, $h$ -Planck's constant, h$\nu$ - photon energy, $Eg$ band gap. The band gap of fabricated photocatalysts were determined using Kubelka-Munk Eq. (5):

$$a = \frac{(1-R)^2}{2R} \tag{5}$$

From the KM function the calculated direct band gap (Eg) values were 2.43 eV for $Cu_2O$-A, 2.48 eV for $Cu_2O$-B, 2.21eV for $Cu_2O$-C and 2.01eV for $Cu_2O$-D respectively. Here, the $Cu_2O$-B greatly influenced the valency band and conduction band energy levels, which could be due to the strong interfacial connection between CuO and $Cu_2O$ core-shell. The synthesised core-shell CuO@$Cu_2O$ photocatalysts phase purity and crystallinity was characterized by PXRD **(Fig.1b)** and the volume-average crystalline size calculated using by Scherrer equation **(Table 1).** The diffraction 2θ values of $Cu_2O$-A were 29.62°, 32.4°, 36.48°, 39.48°, 42.34°, 50.18°, 53.57°, 61.48°,68.49° and 73.42°, and corresponding d-spaces were 3.01(ang), 2.76 (ang), 2.46(ang), 2.26 (ang), 2.13 (ang), 1.81 (ang), 1.70 (ang), 1.51 (ang), 1.36 (ang), and 1.29 (ang), respectively, all assigned peaks observed mixture of $Cu_2O$, CuO, and Cu phase. $Cu_2O$-B 2θ at 29.68°(d=3.0), 30.90 (d=2.9), 32.43°(d=2.75), 35.46°(d=2.52), 36.5°(d=2.46), 38.65(d=2.32), 39.82°(d=2.26), 42.38°(d=2.13), 50.29°(d=1.81), 53.68°(d=1.7), 61.40°(d=1.5), 68.22°(d=1.37) and 73.42°(d=1.28), corresponding PDF card numbers were 01-078-2076 ($Cu^+$), 01-073-6372, 01-087-0679($Cu^{2+}$), and 01-07-3038 (Cu) phase, respectively[13, 24].

**Table 1** Physicochemical characterizations of Core-Shell CuO@$Cu_2O$ photocatalyst

| Catalyst | Crystalline size /nm[a] | BET surface area[b] / m$^2$.g$^{-1}$ | Band gap /eV[c] | VB edge potential/eV [d] | CB edge potential/eV [d] | Average particle size/ nm TEM[e] |
|---|---|---|---|---|---|---|
| $Cu_2O$-A | 11.8 | 24.72 | 2.43 | 1.18 | -1.25 | 240-300 |
| $Cu_2O$-B | 37.1 | 21.34 | 2.48 | 1.12 | -1.36 | 350-500 |
| $Cu_2O$-C | 13.1 | 17.56 | 2.21 | 0.91 | -1.30 | 350-400 |
| $Cu_2O$-D | 52.0 | 12.31 | 2.01 | 0.83 | -1.27 | 2700 |

[a] XRD. [b] N2 porosimetry. [c] DRUVS. [d] calculated from valence band XPS and DRUVS. [e] Cu 2p XPS. [f] TEM

To further prove core -shell structure by PXRD using d-spacing values were 1.81 A° corresponding to (200) plane of Cu core, whereas the inner shell/first shell d-space is 2.46 A° corresponding to (111) plane for $Cu_2O$[25]; and the second shell/outer shell d-space is 2.52 A° corresponding to (111) plane for

CuO[17], which is further proved by STEM and Electron energy loss spectroscopy (EELS). PXRD patten of $Cu_2O$-C was assigned all $2\theta$ values indicated only pure $Cu_2O$ phase, no other impurity reflections were observed during 30 min reaction, due to reducing agent concentration (0.5mL) and controlled addition of reagents, first sodium hydroxide and then reducing agent.

Further to prove the core and shell $CuO/Cu_2O$ architectures and the particle distributions by scanning transmission electron microscopy and transmission electron microscopy. The uniform distributions of core-shell $CuO/Cu_2O$ architectures from low hydrothermal template free morphology at higher and lower magnification clearly evidenced by STEM showed **Fig.2 a-d (**higher magnification**) and Fig. S2 (**lower magnification**),** and the distribution of Cu and oxygen species in the $Cu_2O$-B catalyst further confirmed by elemental mapping at lower magnification (**Fig.2 e-f**). The STEM images clearly showed smaller hollow and broken particles in $Cu_2O$-A, which is due to amount of hydrazine monohydrate (0.5mL). Whereas, bigger particles observed in $Cu_2O$-D is due to amount of PEG (0.5mL) and Cu (II)-less PEG complex with $H_4N_2.H_2O$, indicated the complete self-aggregation small particles in too bigger. The core-shell CuO and $Cu_2O$ and presence of small amount Cu species in $Cu_2O$-B further evidenced with lattice interplanar spacing of 2.52 Å, 2.46 Å, 1.81 Å (**Fig. 2j** and **Fig. 2g** insert), which is corresponding to (111), (111), (200), and lattice planes of CuO, $Cu_2O$ and Cu species consisted with XRD results and reports[4, 17, 26].
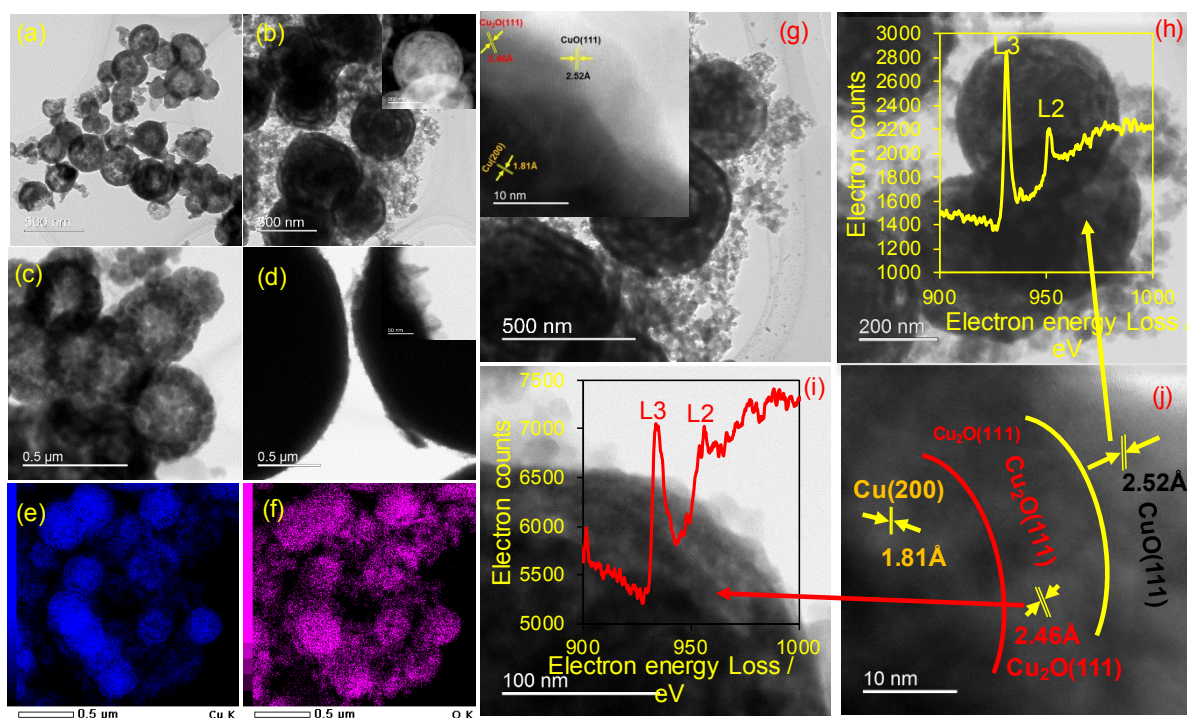


**Fig.2** STEM images of a) $Cu_2O$-A, b) $Cu_2O$-B, c) $Cu_2O$-C, d) $Cu_2O$-D, e and f) $Cu_2O$-B elemental mapping, g-j) STEM images of $Cu_2O$-B at different magnifications, and electron energy loss spectroscopy (embedded) (h-and i).

From STEM images, the core-shell formation clearly evidenced that the smaller unit nanoparticles started self-aggregation followed by nucleation growth to integrated lager unit's with size distributions around 350 to 500 nm. The electron energy loss spectroscopy (EELS) provides sensitive chemical environment and the fine structures of the atoms, the lines shape is different for metallic copper than oxygen surrounded Cu in the CuO and $Cu_2O$. Here, the location of $Cu^+$ and $Cu^{2+}$ species were confirmed by EELS beam focused on different surface locations in $Cu_2O$-B catalysts (**embedded in Fig.2h and i**), indicated that the line shapes and edges of L2, and L3 ratios were different from CuO than $Cu_2O$ [27]. Additionally, EELS spectrum of CuO line shapes CuL3 and CuL2 showed lower curve than $Cu_2O$, which clear information on the different species as well as the location of two species, and $Cu^0$ does not have any line shapes, due to filled conduction band consisted with reports[28, 29]. The structural characterization showed the existence of $Cu^{2+}$ species in the form of CuO at the surface played an important role to control the kinetic stabilization rates of $Cu_2O$ to further oxidation [30]. Field emission scanning electron microscopy images of fabricated core-shell CuO/$Cu_2O$ photocatalysts at higher and lower magnification presented **Fig. 3a-d (**higher magnification**) and Fig. S3** (lower magnification). The core-shell architectures were formed by hundreds of smaller CuO units (first layer) followed by $Cu_2O$ (second layer) are aggregated differently like cauliflower morphologies due to structure directing agents, time heavily influenced the nucleation growth of particles with distribution rages from 300 to 500 nm (**Fig.3a-d,** insert). While, the amount of structure directing agent controlling particle sizes, consisted with our previous report[4].
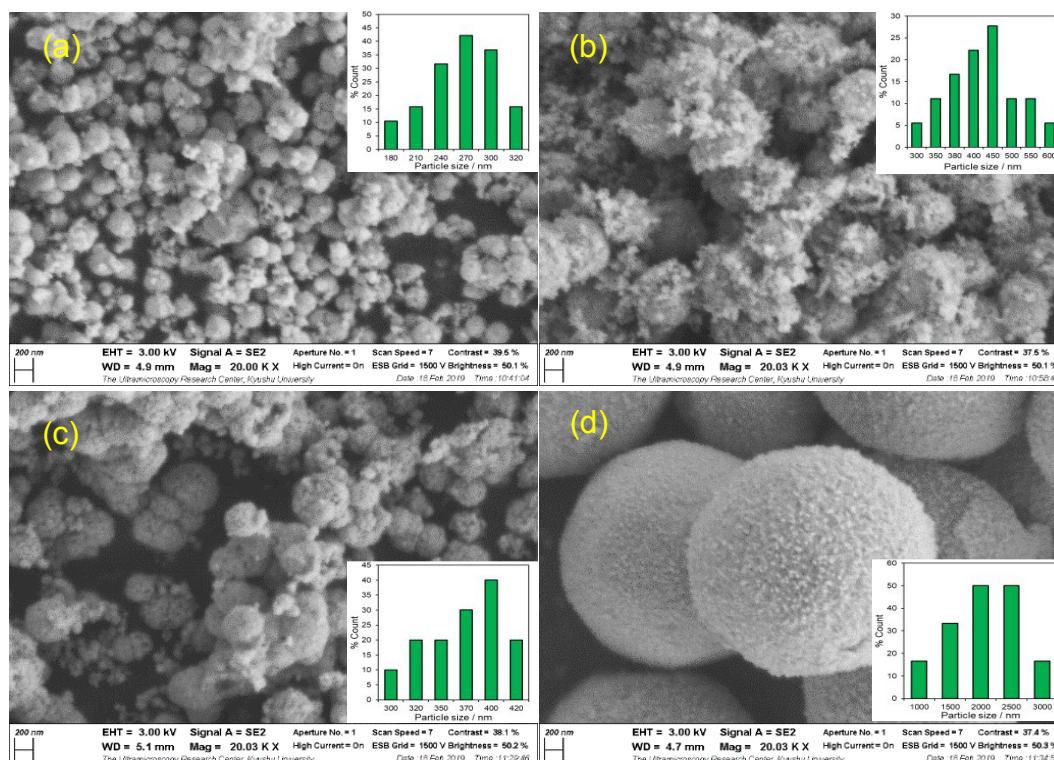


**Fig. 3** Higher magnification FE-SEM images of a) $Cu_2O$-A, b) $Cu_2O$-B, c) $Cu_2O$-C, d) $Cu_2O$-D

The core-shell CuO/Cu$_2$O formation described by self-transformation methods of agglomerated smaller units together by the localized Ostwald ripening[31]. Similar size (~400 nm) and structures (different core-shell) controlled was achieved by H-terminated p-type Si (100) substrate using electrodeposition techniques[15]. The formation of core shell/ hollow spheres due to the PEG initially formed micelles when heated the reaction mixture and the copper-hydroxyl species formed by electrostatic interaction between Cu$^{2+}$ and OH$^-$, which direct to improve copper (II) spices and interface between hydrophilic (OH) groups in PEG in the reaction mixture. Copper (II) spices reduced to Copper (I) oxide by Ostwald ripening processes[20].

The surface oxidation states of fabricated core-shell CuO/Cu$_2$O photocatalysts were examined by copper core level Cu2p X-ray photoelectron spectroscopy presented in **Fig.4a.** The surface Cu$^+$ and Cu$^{2+}$ species played important role in the present photocatalytic system, the observed strong main binding energy peaks at 931.7 ± 0.5 eV and 951.6 ± 0.2 associated to spin-orbit split of Cu2p$_{3/2}$ and Cu2p$_{1/2}$ peaks in Cu/Cu$_2$O, and the existence small amount metallic coper evidenced from XRD. The strong shakeup satellite at higher binding energy of 937.4 eV and 957.2 eV (along with weak 941 eV satellite feature), peaks in both Cu$_2$O-B and Cu$_2$O-D corresponds to CuO[26] (core surface) consisted with TEM d-spacing result.
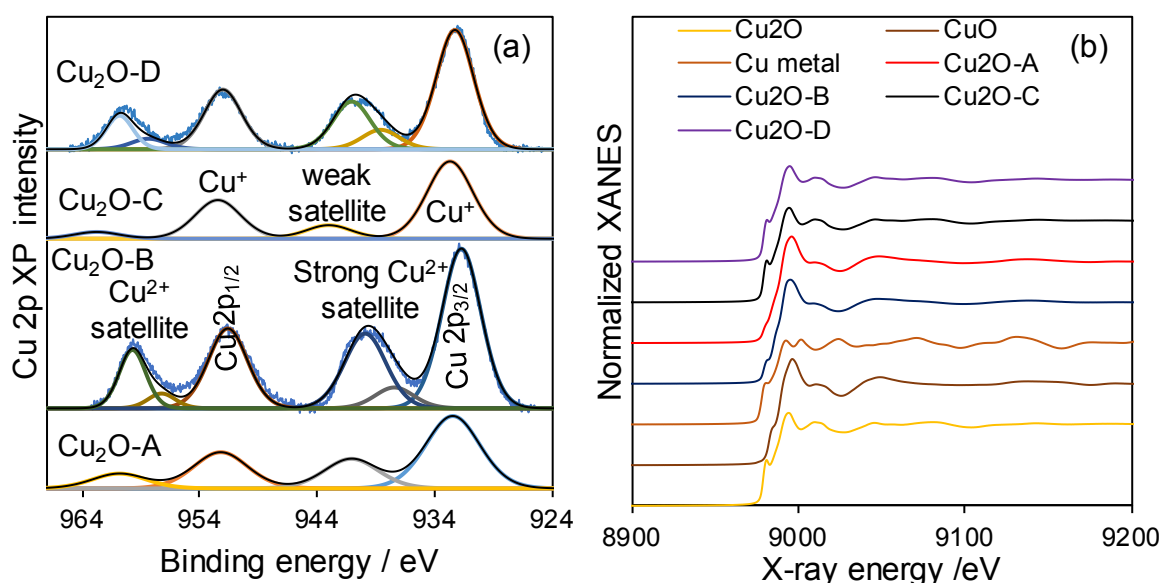


**Fig. 4** a) Cu2p XP spectra (spectra offset for clarity), b) XANES spectra of standard and synthesised catalysts

The characteristic of strong shakeup features corresponds to incompletely occupied 3d$^9$ shell arrangement of Cu$^{2+}$ species at outer shell surface, and existence of CuO shell prevent the stability of Cu$_2$O surface to further oxidation[19]. Further to confirm the oxidation potentials of the fabricated core-shell CuO/Cu$_2$O archistructures by electronic valency band maximum from intercept of tangent by VB XP spectra **(Fig.S4).** The VB edge potential of Cu$_2$O-A (1.18 eV) and Cu$_2$O-D (0.83 eV) decreased due

to increasing particle size, similar phenomena was observed our previous report[4].The conduction band potential determined from VB edge potentials and the calculated CB potentials values are -1.25 eV for $Cu_2O$-A, -1.36 eV for $Cu_2O$-B, -1.30 eV for $Cu_2O$-C, and -1.27 eV for $Cu_2O$-D, which is significantly higher than the required reactive oxygen species potentials (−0.16 (E0) [V] at pH 7)[32]. XANES spectra provide bulk information about presence of $Cu^0$, $Cu^+$ and $Cu^{2+}$ species in the synthetic composite samples, which are challenging to describe $Cu/Cu_2O$ phases from XPS and other techniques. We have performed Cu K-edge XANES analysis of $Cu_2O$-A to $Cu_2O$-D catalysts, which is compared with standard Cu-metal, $Cu_2O$ and CuO and confirmed the oxidation states as well as the quantitative compositions by linear combination fitting (LCF). The XANES spectra of $Cu_2O$-B catalysts absorption edge energy observed values were 8978.4, 8978.9 and 8982.4 eV, corresponding characteristic features of Cu ($3d^{10}4s$, $1s\rightarrow4p$), $Cu^+$ ($1s \rightarrow 4p_{x,y}$) and $Cu^{2+}$($1s\rightarrow3d$)[33], which is compared with $Cu_2O$-A to $Cu_2O$-D (**Fig.4b).** The quantitative phase percentages of synthesised catalysts obtained from normalized absorption near edge by LCF method presented in **Table 2.**

**Table 2** Copper phase composition of synthesised catalysts by XANES using LCF analysis

| Catalyst | Copper I / % | Copper II /% | Cu /% | Cu I /Cu II | R-factor |
|----------|--------------|--------------|-------|-------------|----------|
| **Cu₂O-A** | 13.8 | 84.7 | 1.5 | 0.16 | 0.0030 |
| **Cu₂O-B** | 22.1 | 75.8 | 2.1 | 0.29 | 0.0042 |
| **Cu₂O-C** | 84. 6 | 15.4 | - | 5.49 | 0.0002 |
| **Cu₂O-D** | 81.3 | 18.7 | | 4.34 | 0.0008 |

As we expected the $Cu_2O$-A and $Cu_2O$-B catalysts showed majority of CuO phase along with $Cu_2O$ and Cu phase. While, $Cu_2O$-C and $Cu_2O$-D showed majorly $Cu_2O$ phase and small amount of CuO phase percentage. The quantitative XANES results confirmed the $Cu_2O$, CuO, and the Cu phase mixtures almost which are in good agreement with the XRD results.

Surface textural properties synthesised core -shell $CuO/Cu_2O$ architectures determined by $N_2$ porosimetry showed type II adsorption-desorption isotherms with small H3-type hysteresis loops (**Fig. S5**). Specific surface area of the synthesised core-shell/ hollow $CuO/Cu_2O$ structures determined from BET measurements and the results were 24.72 $m^2$ $g^{-1}$ (for $Cu_2O$-A), 21.34(for $Cu_2O$-B), 17.56 $m^2$ $g^{-1}$ (for $Cu_2O$-C), 12.31 $m^2$ $g^{-1}$ (for $Cu_2O$-D), respectively. Surface areas were decreased with increasing time due to particle aggregations and size effect. Off course, the smaller sizes catalysts are efficient in photocatalytic processes because of high reactive surface area. But, other surface factors (e.g. electron

mobility between heterojunctions, inhibited charge recombination, and surface termination) may favour bigger nanostructures[34].

### 3.1. Photocatalytic APAP oxidation

Here, the selected N-acetyl-para-aminophenol (APAP) as a model organic pharmaceuticals compound has great attention in aqueous contaminants because presence of these huge amount, analgesics, antibiotics, anti-inflammatories, lipid regulators, and anti-epileptics in wastewaters (concentration levels ng $L^{-1}$ to µg $L^{-1}$), including ground and drinking water[26]. In Japan, 41 pharmaceuticals and phytochemicals and the concentration ranges from ng/L to µg/L, with highest level of 92 µg/L found in hospital wastewater[35]. Among the drugs, the N-acetyl-para-aminophenol is one of the most heavily used humans and animal drugs in overall the world as an antipyretic and analgesic, and the concentrations levels in 6 µg $L^{-1}$ in Europe sewage treatment plant, 10 µg $L^{-1}$ in USA natural water[36], and more than 65 µg L-1 in the Tyne river in the United Kingdom[37].
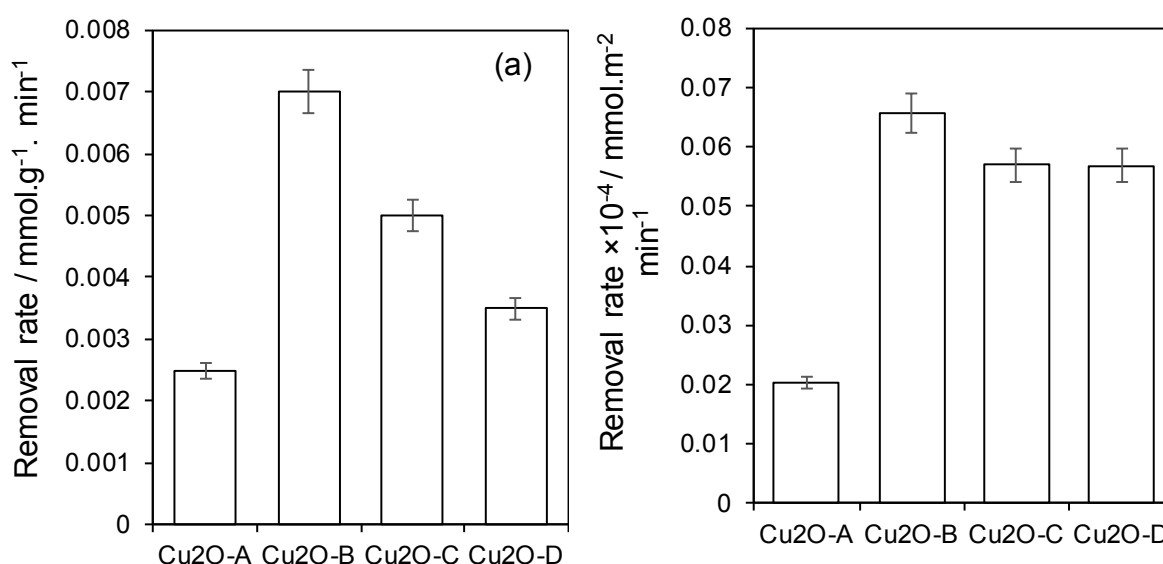


**Fig. 5** N-acetyl-para-aminophenol (APAP) removal rate by fabricated core-shell CuO@Cu$_2$O photocatalyst under visible light, a) initial removal rate, b) area normalised rate (Experimental conditions: 0.06 mmol APAP in 50 mL water, 20 mg catalyst, visible light source cut-off filter 420 nm, 90 min reaction)

According to **Kim et. al.** in South Korea the surface and STP water concentration of 0.033 and 6.8 µg $L^{-1}$ [38], 1.7 µg/L in WWTPs effluent in Japan[39]. The importance of N-acetyl-para-aminophenol is chosen because no visible light region absorbance properties, and it will not affect the genuine photocatalytic efficacy [40]. Here, we have systematically studied the different core-shell/ hollow CuO/Cu$_2$O photocatalyst for APAP photodegradation under visible light. The adsorption capacity of the

synthesised photocatalysts were performed in dark at 1h, and negligible amount of adsorption observed and light only photoreaction showed only 3.6 %. The photocatalytic efficiency of the fabricated catalysts was performed for APAP decomposition and the initial removal rates of 2.5, 7.0, 5.0, and 3.5 $\times 10^{-3}$ / mmol. $g^{-1}$. $min^{-1}$ for $Cu_2O$-A, $Cu_2O$-B, $Cu_2O$-C and $Cu_2O$-D, respectively, while the surface area normalized rates of 0.02, 0.065, 0.057 and $0.056 \times 10^{-4}$ / mmol. $m^2$. $min^{-1}$ for $Cu_2O$-A to $Cu_2O$-D under visible light presented **Fig.5 a-b.**

Upon visible light illumination on core-shell photocatalysts, the initial and surface area normalized rates of $Cu_2O$-A and $Cu_2O$-B catalysts were direct relationship with APAP photooxidation, and $Cu_2O$-B photocatalyst showed enhanced photocatalytic performance than other family of catalysts, which is due to the influence of either surface core-shell $Cu^+$, $Cu^{2+}$ species or bulk electronic properties. Additionally, the strong interfacial contact between $CuO$-$Cu_2O$ architectures, which is responsible to facilitate the charge transfer performance and the role of Cu species acted electron trapping tendency that can effectively separate charges form photoinduced electron and hole pairs.
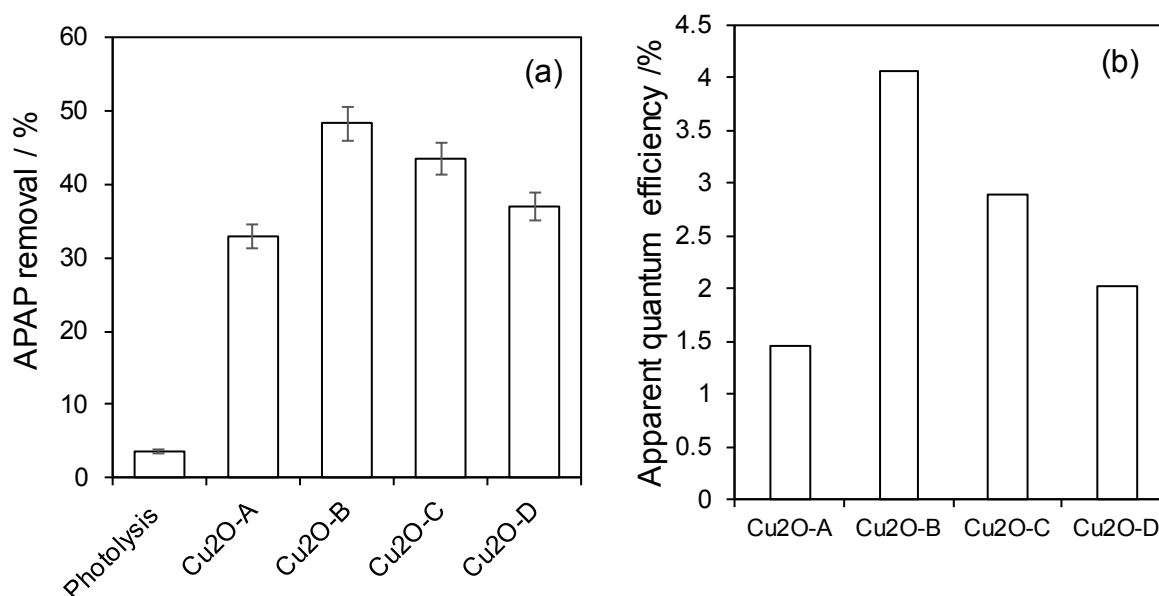


**Fig. 6** a) N-acetyl-para-aminophenol (APAP) removal percentage over core-shell photocatalyst under visible light (Experimental conditions: 0.06 mmol APAP in 50 mL water, 20 mg catalyst, visible light source cut-off filter 420 nm, 300 min reaction.), b) corresponding apparent quantum efficiency.

The higher photocatalytic efficiency not only lower recombination of charges evidenced by solid state PL, but also several scatting effect inside the shell and to absorb more number of photons[41]. The photocatalytic APAP removal efficiency was compared with other family of photocatalysts **(Fig.6a)**, the higher efficiency of $Cu_2O$-B catalyst due to active surface of $CuO$, $Cu_2O$, effective solar light harnessing, and lower recombination properties to enhance the charge transfer facilities longer time for improved photocatalytic performance. Apparent quantum efficiencies calculated from rates of APAP

degradation (**Fig. 6b**), and Cu$_2$O-B catalysts showed 2-fold higher than other family of photocatalysts. The photocatalytic degradation performance of APAP over core-shell CuO/Cu$_2$O compared with other bench mark photocatalysts (neither reported apparent quantum efficiency) in terms of light source and mass of catalysts (**Table S1; references S1-S6**), and the rates of synthesised catalysts significantly higher than alternative semiconducting photocatalyst. The enhanced photocatalytic performance was further evidenced by the charge separation and recombination properties. Photo luminance spectra (excitation @380, and 572nm) and the emission were recorded 420, 572 nm and 616 nm of synthesised photocatalyst (**Fig.7a-b**), confirmed the recombination properties, the slower radiative recombination presence of Cu species may accelerate the valency and conduction band positions, and trap electrons from the photoexcited electron-hole pairs for higher photocatalytic activity[42-44].
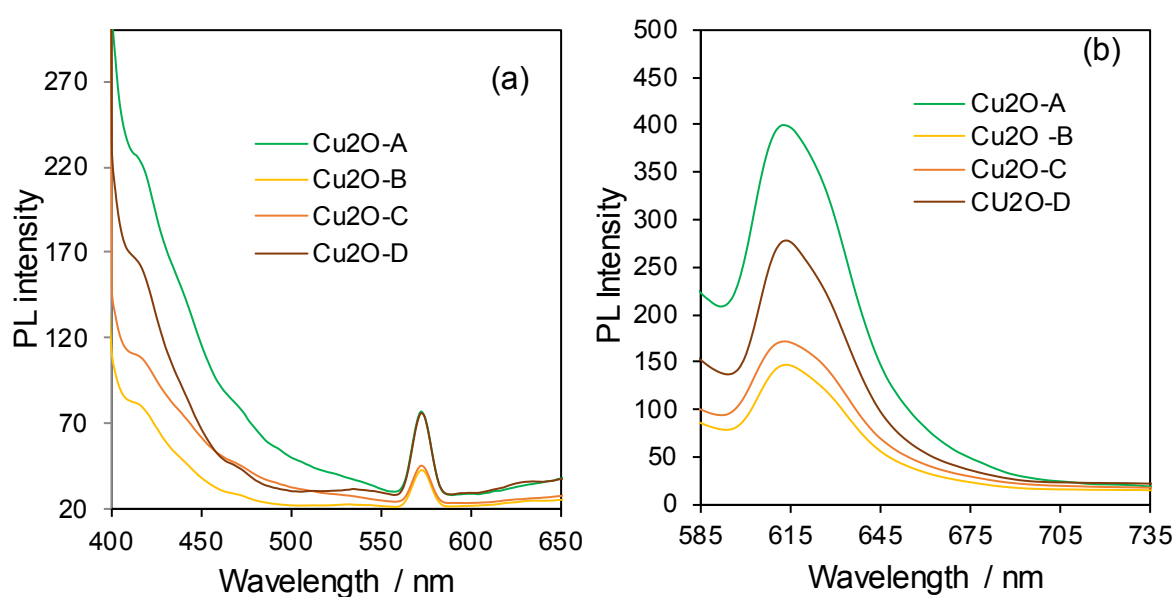


**Fig.7** Recombination properties by PL emission spectra; a) excitation @380 nm and Emission @420, 572nm, b) excitation @560 nm and emission @616 nm (experimental conditions; band width (ex):3nm, band width (em):10nm, Response 0.5 sec, PMT Voltage 900 V, Scan speed 200 nm/min).

Verified the charge separation and recombination properties by PL spectrum, it can be observed the weak PL intensity in Cu$_2$O-B catalyst clear indication about the suppressing recombination of charges from photoinduced electron and hole pairs. The lower recombination property in the catalysts showed higher photocatalytic activity, due to small amount of Cu species as receiver of electrons from surface Cu$_2$O and CuO acts as an electron transfer sites and stabilize the Cu$_2$O to further oxidation may advantages for efficient photocatalytic applications. The APAP decomposition over core-shell CuO/Cu$_2$O photooxidation by-products were determined using HPLC, negligible intermediate compounds were detected initially in our experiment, may be due to separation of these organics by the solvent system or fast intermediates conversation into another products.
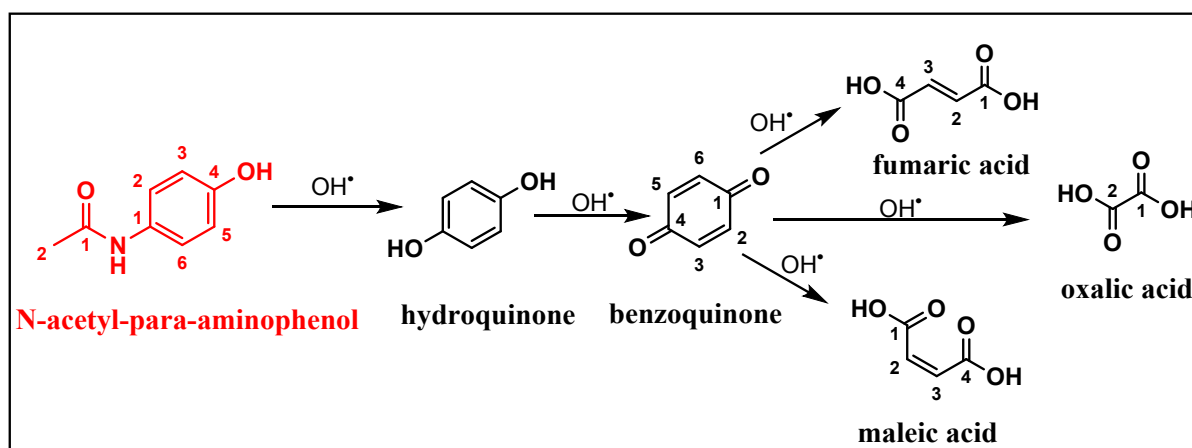
**Scheme 2:** Schematic by-products formation during our photocatalytic reaction.

However, the final reaction mixtures we observed some intermediates such as lower molecular weight aromatics as well as short chain organic acid intermediates (hydroquinone (HQ), benzoquinone (BQ), fumaric acid (FA), maleic acid (MA) and oxalic acid (OA)) by standard calibration from HPLC provided **Fig.S6 and Scheme 2.** The formation of intermediate species from APPA photocatalytic oxidation is due to cleavage of benzene ring and subsequent hydroxyl radical attack may produce carbon dioxide and water molecules in the reaction system[45]. The photocatalytic APAP degradation pathway by reactive species and ꞏOH radicals attack following route, the APAP mineralization via hydroxyl radicals attach on the aromatic ring in para position respect with -OH in APAP, and initially hydroquinone oxidation with hydroxyl radicals to form benzoquinone, and then further oxidation with hydroxyl radicals to ring opening mechanism produced dicarboxylic acids, consisted with previous report[46].
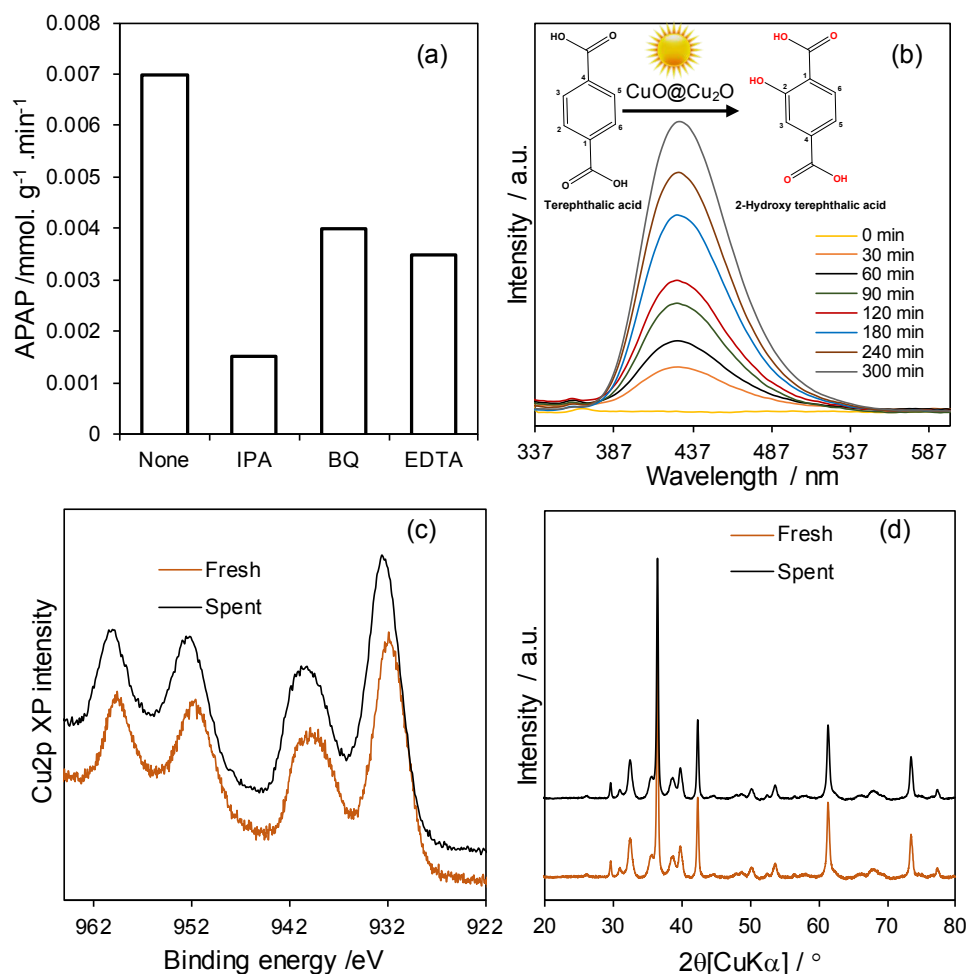
14

**Fig. 8a)** APAP removal rates using scavengers, b) hydroxyl radicals trapping by PL spectroscopy, c) Cu 2p XP spectra of Cu$_2$O-B before and after photoreaction with APAP (20h), d) XRD pattern of Cu$_2$O-B before and after APAP photodegradation (20h)

Furthermore, influencing reactive species for APAP photodegradation performances in the system confirmed by scavenging effects using benzoquinone (BQ), isopropyl alcohol (IPA), and disodium ethylenediaminetetraacetic acid (EDTA) for superoxide radicals (O$_2$$^{•-}$), hydroxyl radicals ($^•$OH), and holes (h$_{vb}$$^+$). **Fig. 8a** showed that the APAP removal rate is 0.007 mmol.g$^{-1}$.min$^{-1}$ higher when no scavengers used, while the removal rate decreased 0.0015, 0.004, 0.0035 mmol.g$^{-1}$.min$^{-1}$, when introducing IPA, BQ and EDTA scavengers, suggesting that a greater number of hydroxyl radicals ($^•$OH) formation heavily influenced APAP photodegradation performances and the influencing order IPA > EDTA >BQ, respectively. Additionally, the formation of superoxide radicals (O$_2$$^{•-}$) in the CuO/Cu$_2$O photocatalytic system, which can further react with water to produce hydroxyl radicals through redox reactions. Furthermore, the radical formation in the APAP degradation mechanisms by CuO/Cu$_2$O with photoinduced reactions with was further established through ($^•$OH) radicals trapping experiment performed by fluorescence spectroscopy using terephthalic acid (TA) as probe molecule.

15

Upon light illumination, the TA reacts with $CuO/Cu_2O$ system to produce $^\bullet OH$ radicals to produce 2-hydroxyterephthalic acid (HTA) in the reaction mixtures, corresponding fluorescence characteristic emission measured at 425 nm (excitation at 315 nm) presented in **Fig. 8b.**
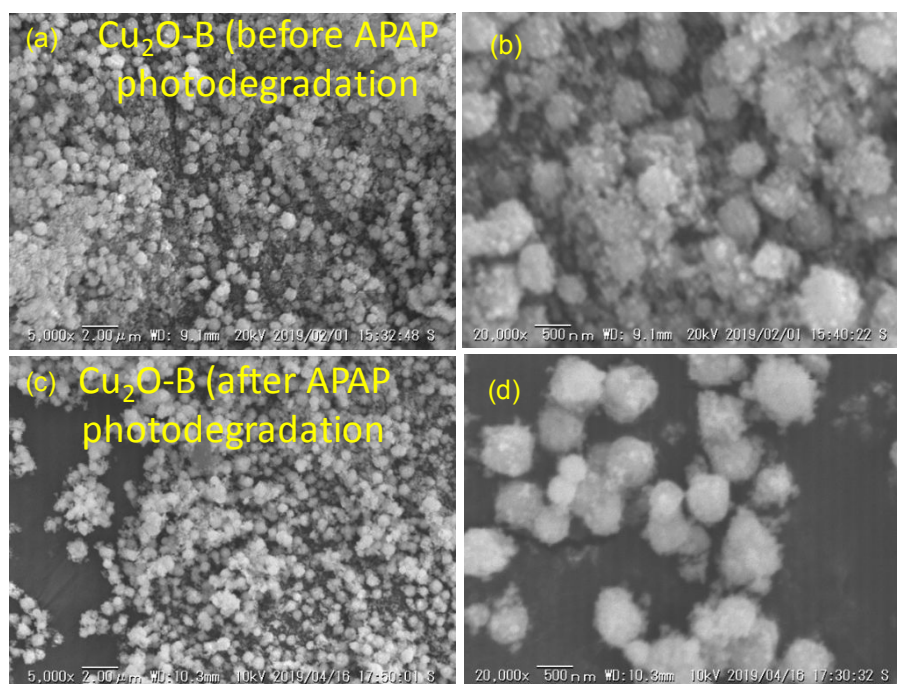


**Fig. 9** SEM of $Cu_2O$-B before (a-b) and after (c-d) photoreaction with APAP (20h).

Results suggest that the hydroxyl radical formation increased with illumination time using $CuO/Cu_2O$ photocatalytic system. The reusability and stability of the catalyst is important issues in the long-term application. Catalyst stability towards APAP photodegradation under visible light was assessed for the $CuO/Cu_2O$ over four cycles showed negligible activity loss during reactions **(Fig. S7),** and the initial surface and crystallinity properties retained, confirmed from XPS and XRD **(Fig. 8c and d).** Hence, the synthesised catalysts showed excellent surface and long-term stability. Additionally, **t**he structural stability of spent catalyst was determined by SEM, resulting photocatalyst core-shell structure well preserved in the post photocatalytic reaction mixture, and there is no structural deformation was observed from SEM after 20h reaction with APAP **(Fig.9 a-d)**. Thus, synthesised $CuO/Cu_2O$ core shell structured catalyst for potential high photocatalytic stability for the removal organics from pharmaceuticals wastewater, not limited solar-driven photocatalytic energy conversion applications.

### 3.2. Photocatalytic APAP removal Mechanism

Photocatalytic APAP degradation over core-shell $CuO@Cu_2O$ mechanism under visible light is proposed based on CB and VB positions and the band alignment **(Scheme 3, supporting information)**. The band gaps of $Cu_2O$ (1.9 to 2.4 eV), CuO (1.2 to 1.5 eV) and both $Cu^+$ and $Cu^{2+}$ oxides have tendency

to adsorb wider range solar spectrum and produce photogenerated electrons and holes [19, 47]. The photogenerated electron and hole charge carriers and migration based on adjacent materials with strong interfacial connection responsible for controlling the charge transport and electron trapping tendency to minimize the charge recombination property for prolong photoreaction. Similar observation **Chen et al 2013 reported**, existence of Cu species played important role for trapping electrons from photoexcited $Cu_2O$ electrons and higher charge separation to minimize recombination property for enhanced photocatalytic efficiency prolong time [48]. The valency band (+1.12 eV) and conduction band (-1.36 eV) positions of $CuO@Cu_2O$ are located below the valence band (+2.16 eV) and conduction band (+0.46 eV) vs. normal hydrogen electrode (NHE) of CuO [49]. The band energy alignment of core-shell $CuO/Cu_2O$ architectures strong evidenced that the photogenerated electrons transferred to conduction band of CuO from $Cu_2O$, leaving positive holes in CuO transferred to valency band of $Cu_2O$[16], and Cu species in the network accept photogenerated electrons from conduction band of $Cu_2O$ to avoid the recombination property. The electron-hole pair charge recombination is significantly inhibited in core-shell $CuO@Cu_2O$ system (which is confirmed by PL spectrum), indicated that the charge transport and hole migration is more efficient by photoinduced electrons. Thus, photogenerated charge carriers in the core-shell system efficiently separated and transfer, which results higher photocatalytic efficiency for prolong life time. Moreover, photoinduced electrons and presence of oxygen ($O_2$) in the conduction band of copper oxide able to scavenge to produce superoxide radical anions ($O^{2\bullet-}$), and this superoxide radical reacted with water produce and hydrogen peroxide ($H_2O_2$) from conduction band (CB), holes in the valence band $Cu_2O$ reacted with hydroxyl ions to form hydroxyl radical. The formation of hydroxyl and super oxide radicals is responsible for photo degradation of APAP in the aqueous solution. The different photocatalytic activity $CuO@Cu_2O$ is related to the different electronic, active dominant (111) facets, different specific surface areas, and direct band gaps much influenced the APAP degradation.

## 4. Conclusions

A novel one pot low hydrothermal synthesis of core-shell $CuO@Cu_2O$ efficient visible light photocatalyst, structural stability and mechanistic investigation. We have successfully highlighted the construction of core-shell, hierarchical photocatalyst for efficient organic pollutant decomposition with high stability under visible light and the potential photocatalytic performance was investigated through photophysical, surface/bulk electronic, notably the charge trapping, and charge-separation rates, and apparent quantum efficiency are closely related with surface structure and particle sizes towards APAP photodegradation activity under visible light. Despite their surface-active species controlling the kinetic stability of the $Cu_2O$ to further oxidation and superior APAP photooxidation with excellent stability over 20h reusability confirmed by post reaction catalysts (XPS, XRD and SEM). These results are potential for constructing semiconductors and new insights for photocatalytic environmental remediation and other solar-driven photo/electrocatalytic energy conversion applications.

**Conflicts of interest**
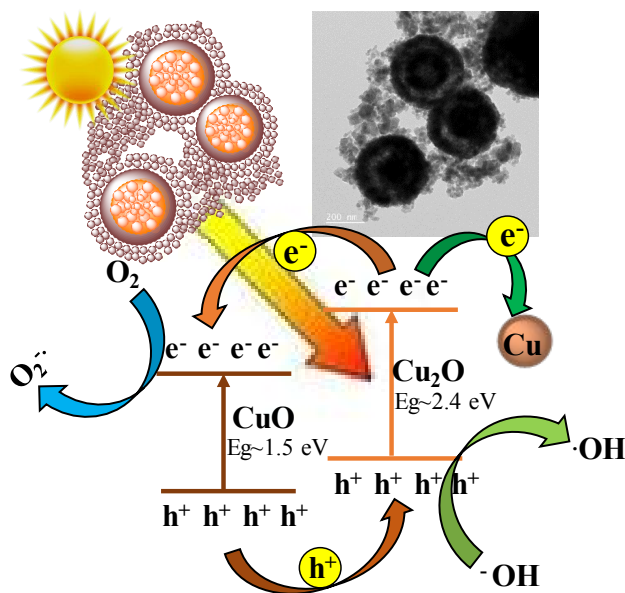
The authors declare no conflict of interest.

**References**

1.      A. Fujishima, T. N. Rao and D. A. Tryk, *Journal of Photochemistry and Photobiology C: Photochemistry Reviews*, 2000, **1**, 1-21.
2.      W.-K. Jo, S. Kumar, M. A. Isaacs, A. F. Lee and S. Karthikeyan, *Applied Catalysis B: Environmental*, 2017, **201**, 159-168.
3.      M. B. Gawande, A. Goswami, F.-X. Felpin, T. Asefa, X. Huang, R. Silva, X. Zou, R. Zboril and R. S. Varma, *Chemical Reviews*, 2016, **116**, 3722-3811.
4.      S. Karthikeyan, S. Kumar, L. J. Durndell, M. A. Isaacs, C. M. A. Parlett, B. Coulson, R. E. Douthwaite, Z. Jiang, K. Wilson and A. F. Lee, *ChemCatChem*, 2018, **10**, 3554-3563.
5.      M. J. Siegfried and K. S. Choi, *Angewandte Chemie International Edition*, 2005, **44**, 3218-3223.
6.      Y. Liu, B. Zhang, L. Luo, X. Chen, Z. Wang, E. Wu, D. Su and W. Huang, *Angewandte Chemie International Edition*, 2015, **54**, 15260-15265.
7.      F. Wang, W. Septina, A. Chemseddine, F. F. Abdi, D. Friedrich, P. Bogdanoff, R. van de Krol, S. D. Tilley and S. P. Berglund, *Journal of the American Chemical Society*, 2017, **139**, 15094-15103.
8.      W.-C. Huang, L.-M. Lyu, Y.-C. Yang and M. H. Huang, *Journal of the American Chemical Society*, 2012, **134**, 1261-1267.
9.      Y. Su, H. Li, H. Ma, H. Wang, J. Robertson and A. Nathan, *ACS Omega*, 2018, **3**, 1939-1945.
10.     Y. Kwon, A. Soon, H. Han and H. Lee, *Journal of Materials Chemistry A*, 2015, **3**, 156-162.
11.     W. Wang, J. Wang, Z. Wang, X. Wei, L. Liu, Q. Ren, W. Gao, Y. Liang and H. Shi, *Dalton Transactions*, 2014, **43**, 6735-6743.
12.     Z. Ai, L. Zhang, S. Lee and W. Ho, *The Journal of Physical Chemistry C*, 2009, **113**, 20896-20902.
13.     J. Kou, A. Saha, C. Bennett-Stamper and R. S. Varma, *Chemical Communications*, 2012, **48**, 5862-5864.
14.     C. C. Yec and H. C. Zeng, *Chemistry of Materials*, 2012, **24**, 1917-1929.
15.     A. Radi, D. Pradhan, Y. Sohn and K. T. Leung, *ACS Nano*, 2010, **4**, 1553-1560.
16.     H. Li, Z. Su, S. Hu and Y. Yan, *Applied Catalysis B: Environmental*, 2017, **207**, 134-142.
17.     W. Chen, Z. Fan and Z. Lai, *Journal of Materials Chemistry A*, 2013, **1**, 13862-13868.
18.     H. Yu, J. Yu, S. Liu and S. Mann, *Chemistry of Materials*, 2007, **19**, 4327-4334.
19.     M. Yin, C.-K. Wu, Y. Lou, C. Burda, J. T. Koberstein, Y. Zhu and S. O'Brien, *Journal of the American Chemical Society*, 2005, **127**, 9506-9511.
20.     H. Xu and W. Wang, *Angewandte Chemie*, 2007, **119**, 1511-1514.
21.     Y. Yang, D. Xu, Q. Wu and P. Diao, *Scientific Reports*, 2016, **6**, 35158.
22.     J. J. Teo, Y. Chang and H. C. Zeng, *Langmuir*, 2006, **22**, 7369-7377.
23.     R. Chen, S. Pang, H. An, J. Zhu, S. Ye, Y. Gao, F. Fan and C. Li, *Nature Energy*, 2018, **3**, 655-663.
24.     Q. Song, W. Liu, C. D. Bohn, R. N. Harper, E. Sivaniah, S. A. Scott and J. S. Dennis, *Energy & Environmental Science*, 2013, **6**, 288-298.
25.     S. B. Kalidindi, U. Sanyal and B. R. Jagirdar, *Physical Chemistry Chemical Physics*, 2008, **10**, 5870-5874.
26.     H. Azimi, S. Kuhri, A. Osvet, G. Matt, L. S. Khanzada, M. Lemmer, N. A. Luechinger, M. I. Larsson, E. Zeira, D. M. Guldi and C. J. Brabec, *Journal of the American Chemical Society*, 2014, **136**, 7233-7236.

27.     L. Chen, S. Shet, H. Tang, H. Wang, T. Deutsch, Y. Yan, J. Turner and M. Al-Jassim, *Journal of Materials Chemistry*, 2010, **20**, 6962-6967.
28.     N. J. Long and A. K. Petford-Long, *Ultramicroscopy*, 1986, **20**, 151-159.
29.     R. D. Leapman, L. A. Grunes and P. L. Fejes, *Physical Review B*, 1982, **26**, 614-635.
30.     V. R. Palkar, P. Ayyub, S. Chattopadhyay and M. Multani, *Physical Review B*, 1996, **53**, 2167-2170.
31.     X. Meng, G. Tian, Y. Chen, Y. Qu, J. Zhou, K. Pan, W. Zhou, G. Zhang and H. Fu, *RSC Advances*, 2012, **2**, 2875-2881.
32.     J. Li, M. Jiang, H. Zhou, P. Jin, K. M. C. Cheung, P. K. Chu and K. W. K. Yeung, *Global Challenges*, 2019, **3**, 1800058.
33.     I. J. Drake, K. L. Fujdala, S. Baxamusa, A. T. Bell and T. D. Tilley, *The Journal of Physical Chemistry B*, 2004, **108**, 18421-18434.
34.     F. Amano, E. Ishinaga and A. Yamakata, *The Journal of Physical Chemistry C*, 2013, **117**, 22584-22590.
35.     T. Azuma, N. Arima, A. Tsukada, S. Hirami, R. Matsuoka, R. Moriwake, H. Ishiuchi, T. Inoyama, Y. Teranishi, M. Yamaoka, Y. Mino, T. Hayashi, Y. Fujita and M. Masada, *Science of The Total Environment*, 2016, **548-549**, 189-197.
36.     M. Skoumal, P.-L. Cabot, F. Centellas, C. Arias, R. M. Rodríguez, J. A. Garrido and E. Brillas, *Applied Catalysis B: Environmental*, 2006, **66**, 228-240.
37.     L. Yang, L. E. Yu and M. B. Ray, *Environmental Science & Technology*, 2009, **43**, 460-465.
38.     S. D. Kim, J. Cho, I. S. Kim, B. J. Vanderford and S. A. Snyder, *Water research*, 2007, **41**, 1013-1021.
39.     T. Okuda, Y. Kobayashi, R. Nagao, N. Yamashita, H. Tanaka, S. Tanaka, S. Fujii, C. Konishi and I. Houwa, *Water Science and Technology*, 2008, **57**, 65-71.
40.     N. Barbero and D. Vione, ACS Publications, 2016.
41.     L. Luo, K. Li, A. Zhang, H. Shi, G. Zhang, J. Ma, W. Zhang, J. Tang, C. Song and X. Guo, *Journal of Materials Chemistry A*, 2019.
42.     I. Mukherjee, S. Chatterjee and N. A. Kulkarni, *The Journal of Physical Chemistry C*, 2016, **120**, 1077-1082.
43.     S. Kumar, M. A. Isaacs, R. Trofimovaite, L. Durndell, C. M. Parlett, R. E. Douthwaite, B. Coulson, M. C. Cockett, K. Wilson and A. F. Lee, *Applied Catalysis B: Environmental*, 2017, **209**, 394-404.
44.     A. Gómez-Avilés, M. Peñas-Garzón, J. Bedia, D. D. Dionysiou, J. J. Rodríguez and C. Belver, *Applied Catalysis B: Environmental*, 2019.
45.     L. Yang, E. Y. Liya and M. B. Ray, *Water research*, 2008, **42**, 3480-3488.
46.     D. Vogna, R. Marotta, A. Napolitano and M. d'Ischia, *The Journal of Organic Chemistry*, 2002, **67**, 6143-6151.
47.     M. Heinemann, B. Eifert and C. Heiliger, *Physical Review B*, 2013, **87**, 115111.
48.     W. Chen, Z. Fan and Z. Lai, *Journal of Materials Chemistry A*, 2013, **1**, 13862-13868.
49.     W. Wang, J. Wang, Z. Wang, X. Wei, L. Liu, Q. Ren, W. Gao, Y. Liang and H. Shi, *Dalton Transactions*, 2014, **43**, 6735-6743.

Table of content



Template free mild hydrothermal fabrication of size-controlled core-shell CuO@Cu$_2$O photocatalyst for *N-acetyl-para-aminophenol* decomposition under visible light

**-Supporting information –**
**Template free mild hydrothermal fabrication of size-controlled core-shell CuO@Cu$_2$O visible light photocatalyst, structural stability and their interfacial charge transfer mechanistic investigation**

Sekar Karthikeyan, [†] Chitiphon Chuaicham, [†] Radheshyam R Pawar, [†] Keiko Sasaki, [†]**\*** Wei Li, [‡] Adam F. Lee,[‖] Karen Wilson,[‖]

[†]Department of Earth Resources Engineering, Faculty of Engineering, Kyushu University, 744 Motooka, Nishiku, Fukuoka 819-0395, Japan
[‡]European Bioenergy Research Institute, Aston University, Birmingham B4 7ET, UK
[‖]Applied Chemistry & Environmental Science, RMIT University, Melbourne VIC 3000, Australia.

\*Corresponding Author
   Prof. Keiko Sasaki, E-mail: keikos@mine.kyushu-u.ac.jp, Tel & Fax: +81-92-802-3338

**Core-Shell CuO@Cu$_2$O Characterization**

Core-Shell CuO@Cu$_2$O photocatalysts were characterized diverse analytical techniques such as powder X-ray diffraction (PXRD) using a Rigaku Ultima IV diffractometer, Japan. Cu Kα X-ray radiation was used at 40 kV at an applied current of 40 mA with 0.02° divergence. Band gap energy (Eg) was estimated using diffuse reflectance spectroscopy (DRS-UVis) by a Shimadzu UV-2450 spectrophotometer equipped with ISR-2200 integrating sphere attachment (Kyoto, Japan, serial no. A106453). Solid state Photoluminescence Spectroscopy (PL) was measured using JASCO F-6600 Spectro fluorometer made in Japan (Model FP-6600DS, Serial number: B011060822). Transmission electron microscopy (TEM) images of core-shell CuO@Cu$_2$O catalysts were imaged using a TEM (JEM-2100HCKM, JEOL, Akishima, Japan). TEM and STEM samples prepared by appropriate amount of catalyst was dispersed ethanol and sonicated for even dispersion and then drop coated using carbon coated copper grid (separately molybdenum grid was used for elemental mapping) and then dried for imaging. X-ray photoelectron spectra (XPS) were collected on an ESCA 5800 (ULVAC-PHI, Inc., Kanagawa, Japan). A monochromatic Al Kα X-ray operated at 200 W was used as a source. The binding energy (*EB*) was calibrated using the C 1s peak at 284.6 eV for the contamination carbon from the apparatus, and peak separation was carried out with Casa XPS software (Version 2.3.16 PR 1.6). The specific surface area (SSA) and pore size distribution of the photocatalysts were determined by Japan BEL-Max, BEL (Osaka, Japan). The degradation products were determined on a JASCO LC-netII/ADC high performance liquid chromatography (HPLC) system PU-2089 plus pump, C0-2065 plus column oven and UV-2075 plus detector equipped with a C18 column (K009450, Shodex, Japan). The eluent consists of 30:70 (v/ v) acetonitrile: water (Wako, Japan) with a flow rate of 0.6mL/min.
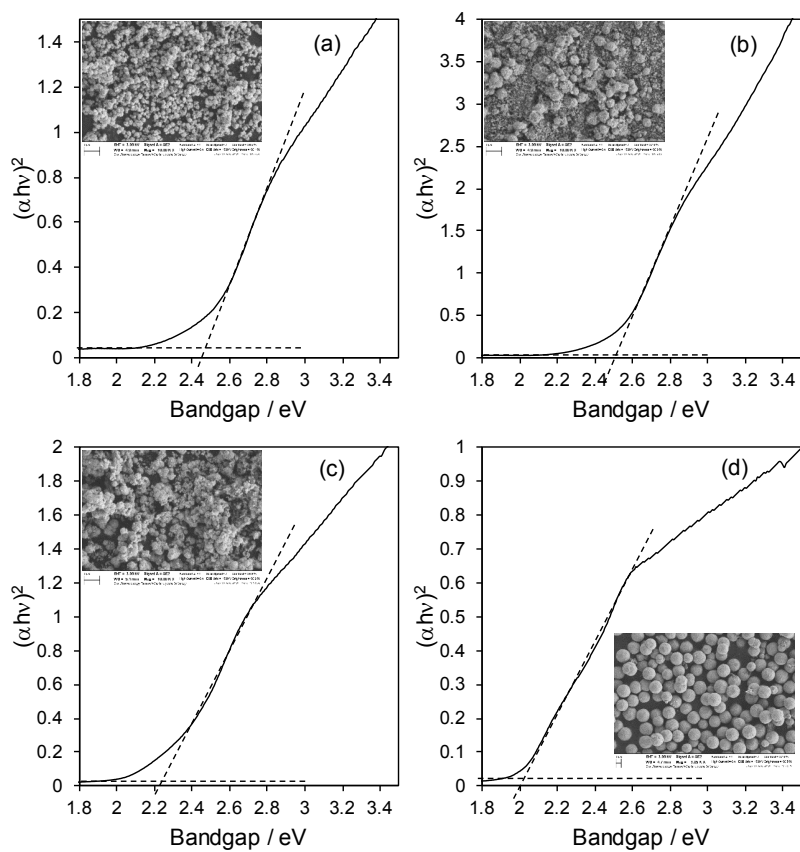
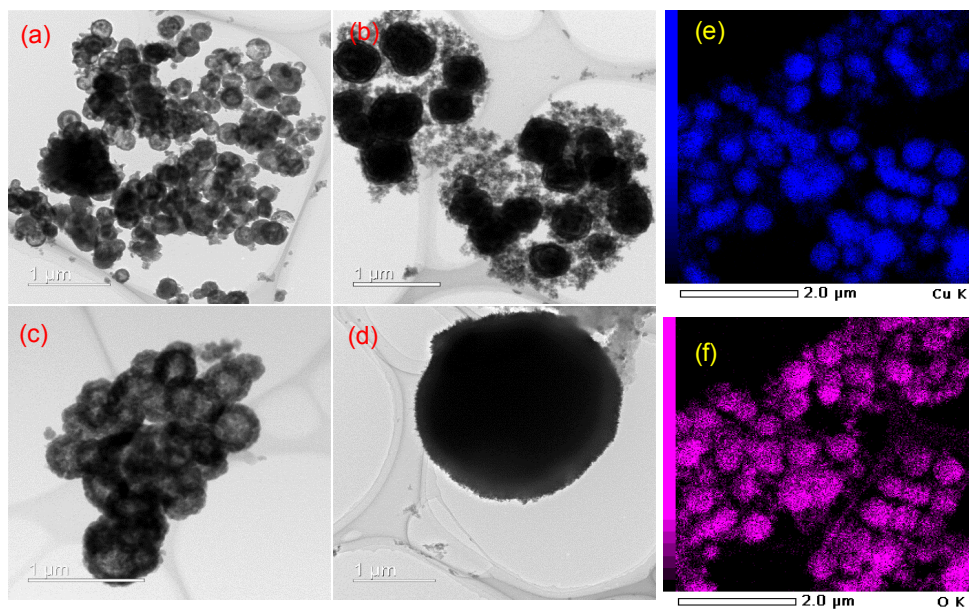**Fig. S1** Solid state DR-UV Tauc plot, a) $Cu_2O$-A, b) $Cu_2O$-B, c) $Cu_2O$-C, d) $Cu_2O$-D



**Fig. S2** Lower magnification TEM images of a) $Cu_2O$-A, b) $Cu_2O$-B, c) $Cu_2O$-C, d) $Cu_2O$-D and lower magnification elemental mapping of $Cu_2O$-B (e and f)
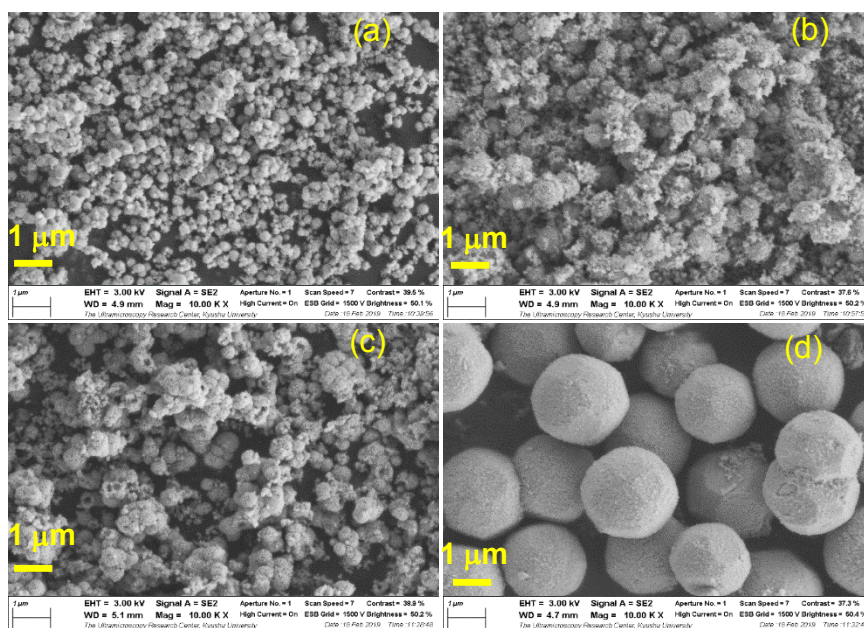
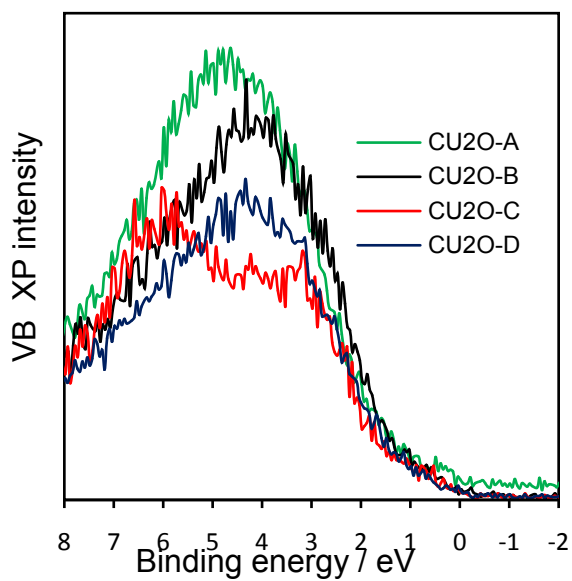**Fig. S3** Lower magnification FE-SEM images of a) $Cu_2O$-A, b) $Cu_2O$-B, c) $Cu_2O$-C, d) $Cu_2O$-D



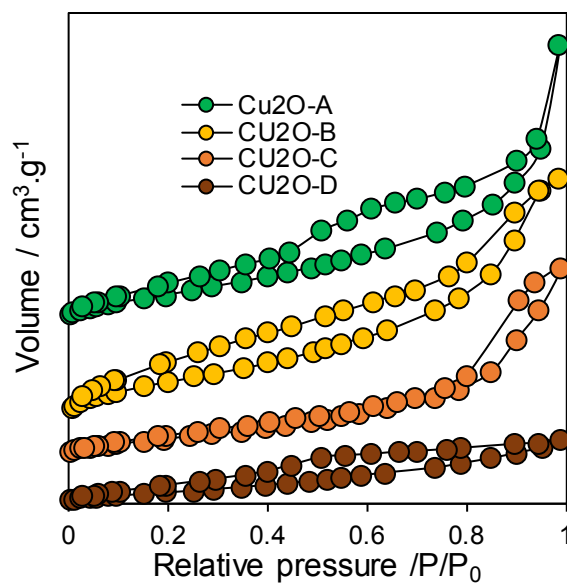**Fig.S4** VB XP spectra of synthesized photocatalyst.

**Fig.S5** $N_2$ adsorption-desorption isotherm of prepared photocatalyst.

**Table S1.** Photocatalytic APAP degradation comparison.

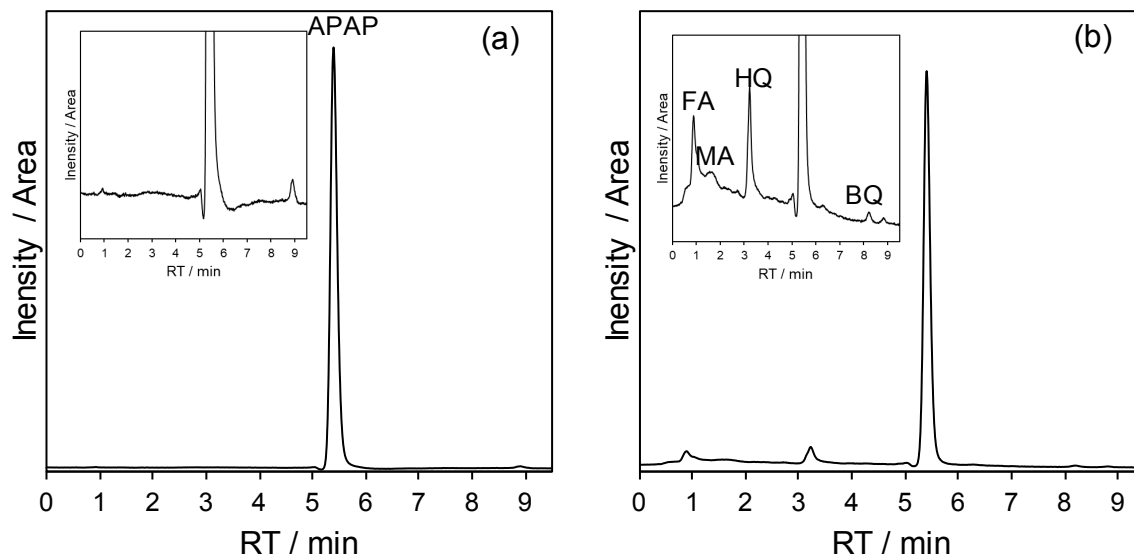| Catalyst | Rate constant / min-1 | Catalyst mass and APAP concentration | Flux of light source | Reference |
|---|---|---|---|---|
| TiO$_2$ | 0.0105 | 0.4 g L$^{-1}$ catalyst, 4μM paracetamol | 15W-UVC lamp (output at 254nm), intensity at 12.6 mW/cm$^{-2}$ | 1 |
| Cu-doped TiO$_2$ | 0.0243 | Photocatalyst 4.0 g/L, APAP 25 mL in aqueous solution | Rayonet RPR-100 photoreactor equipped with 16 visible-light lamps | 2 |
| Platinum-loaded TiO$_2$ | 0.030 | 5mg/L$^{-1}$ catalyst, 40 μM APAP in aqueous solution | photolysis by UVC with low-pressure Hg lamp and intensity at 107.4 W/cm$^{-2}$ (254 nm) | 3 |
| ZnO nanorod | 0.0125 | 100 mg of ZnO, 50 mg/L APAP in aqueous solution, and the active was 1 cm$^2$ | 300 W Xe lamp with external applied bias, UV radiation. | 4 |
| ZnFe -LDH/rGO | 0.00737 | 25 mg catalyst, 50 mL APAP in aqueous solution (5 mg/L) | 500 W xenon lamp with a 300 nm cut-off filter, | 5 |
| Hollow TiO$_2$ microspheres | 0.0448 | 50 mg/L APAP in aqueous solution | 500W Hg-lamp, UV light. | 6 |
| Core-shell CuO/Cu$_2$O | 0.0679 | 20 mg of CuO/Cu$_2$O dispersed 50 mL of APAP (0.06 mM) in aqueous solution | 500 W Xe lamp with a <400 nm cut-off filter, light intensity 1.82 mV/cm$^2$ | Present work |

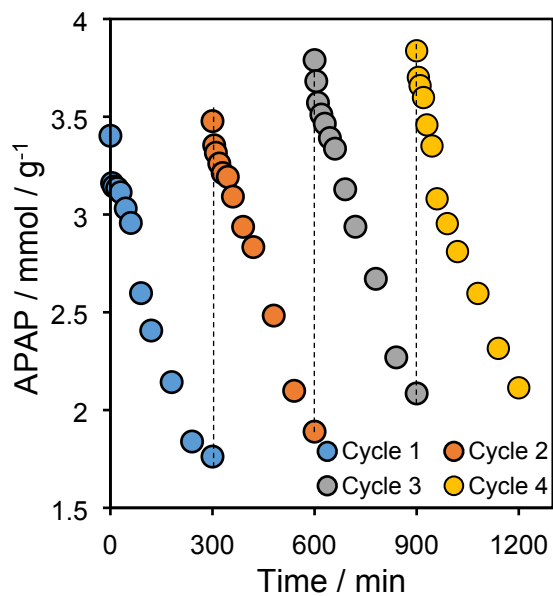**Fig. S6** HPLC of before (a), and after (b) photocatalytic APAP degradation presence of $Cu_2O$-B.



**Fig.S7** Mass normalized APAP decomposition over $Cu_2O$-B (photocatalytic reusability/stability)

**Apparent quantum efficiency (AQE) determination**

The apparent quantum efficiency under visible light irradiation was measured at 420 nm band-pass filter according to the following equations:

$$\text{Apparent quantum efficiency (\%)} = \frac{\text{Mols of reacted electrons per unit time}}{\text{Mols of incident photons per unit time}} \times 100 \qquad (S1)$$

Mols incident photons per unit time $(N_{Einstein})$ = Number incident photons per unit time / $N_A$

Number of incident photons $N_p$ per unit time can be calculated by:

$$N_P = \frac{\text{Intensity (E)}}{\text{Photon energy } (E_p)} \; ; \text{ and } \; \text{photon energy } (E_p) = \frac{hc}{\lambda} \qquad (S2)$$
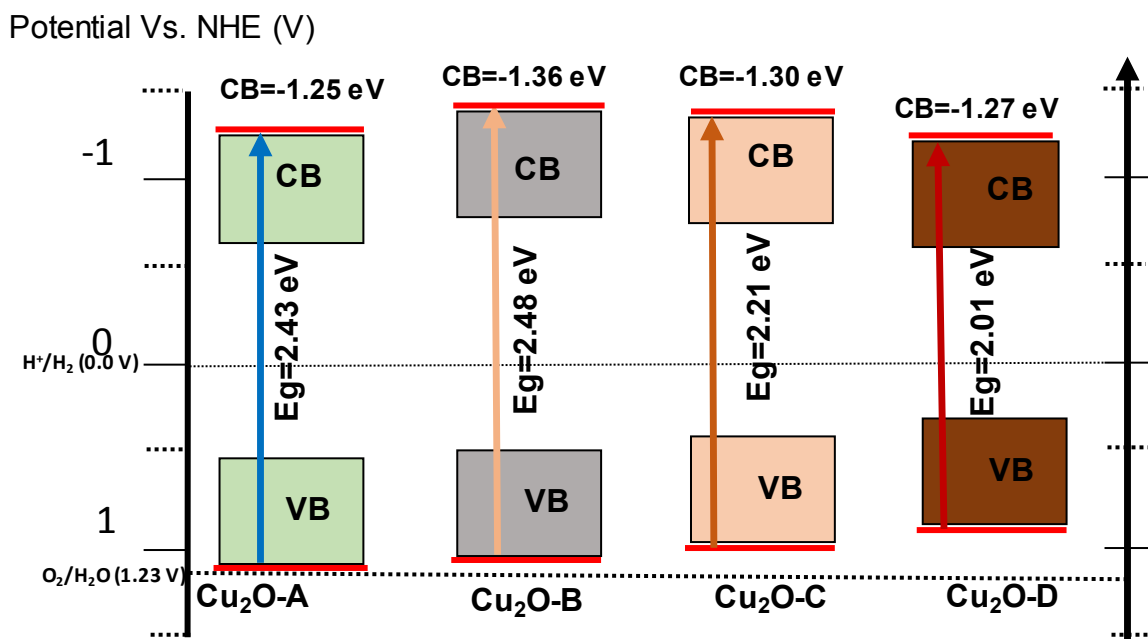
E = Irradiance × reactor area illuminated

$$E_p = \frac{(6.625 \times 10^{-34} \text{ J.s}) (3 \times 10^{17} \text{ nm.s}^{-1})}{\lambda \text{ (nm)}} = \frac{19.88 \times 10^{-17}}{\lambda \text{ (nm)}} = 4.73 \times 10^{-19} \text{ J} \qquad (S3)$$

$$N_p = \frac{E}{E_p} = 0.00819 / 4.73 \times 10^{-19} = 1.73 \times 10^{16} \text{ s}^{-1} \qquad (S4)$$

$$N_{Einstein} = \frac{N_P}{N_A} = 2.87E\text{-}06 \text{ mols.s}^{-1} \qquad (S5)$$

**For phenol photodegradation:**

$$\text{Quantum efficiency (\%)} = \frac{\text{Phenol removal rate}}{\text{Neins}} \times 100 \qquad (S6)$$



**Scheme 3:** Schematic band positions of fabricated a) $Cu_2O$-A, b) $Cu_2O$-B, c) $Cu_2O$-C, d) $Cu_2O$-D

## References

1. L. Yang, E. Y. Liya and M. B. Ray, *Water research*, 2008, **42**, 3480-3488.
2. C.-J. Lin and W.-T. Yang, *Chemical Engineering Journal*, 2014, **237**, 131-137.
3. A. Ziylan-Yavaş and N. H. Ince, *Chemosphere*, 2016, **162**, 324-332.
4. C. J. Lin, S.-J. Liao, L.-C. Kao and S. Y. H. Liou, *Journal of Hazardous Materials*, 2015, **291**, 9-17.
5. J. Zhu, Z. Zhu, H. Zhang, H. Lu, W. Zhang, Y. Qiu, L. Zhu and S. Küppers, *Applied Catalysis B: Environmental*, 2018, **225**, 550-562.
6. C. J. Lin, W.-T. Yang, C.-Y. Chou and S. Y. H. Liou, *Chemosphere*, 2016, **152**, 490-495.